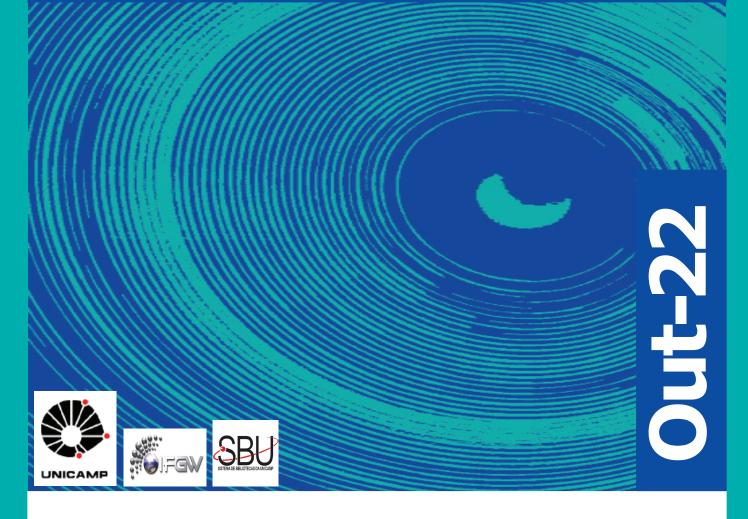
# Abstracta

Ano XXVI - N. 05



Artigos publicados - P211-2022 à P250-2022

Artigos de eventos - P251-2022 à P253-2022

Artigos aceitos para publicação - A002-2022 à A003-2022

Defesas de Dissertações do IFGW - D020-2022 à D025-2022

Defesas de Teses do IFGW - T016-2022 à T022-2022

#### **Artigos publicados**

[P211-2022] "(KSKS0)-K-0 and (KSK +/-)-K-0 femtoscopy in pp collisions at root s=5.02and 13 TeV"

Acharya, S.; Adamova, D.; Chinellato, D. D.\*; Guardiano, G. G.\*; Jahnke, C.\*; Takahashi, J.\*; et al. ALICE Collaboration

Femtoscopic correlations with the particle pair combinations (KSKS0)-K-0 and (KSK +/-)-K-0 are studied in pp collisions at root s= 5.02 and 13 TeV by the ALICE experiment. At both energies, boson source parameters are extracted for both pair combinations, by fitting models based on Gaussian size distributions of the sources, to the measured two-particle correlation functions. The interaction model used for the (KSKS0)-K-0 analysis includes quantum statistics and strong final-state interactions through the f(0) (980) and a(0) (980) resonances. The model used for the (KSK +/-)-K-0 analysis includes only the final-state interaction through the a(0) resonance. Source parameters extracted in the present work are compared with published values from pp collisions at root s = 7 TeV and the different pair combinations are found to be consistent. From the observation that the strength of the (KSKS0)-K-0 correlations is significantly greater than the strength of the (KSK +/-)-K-0 correlations, the new results are compatible with the a(0) resonance being a tetraquark state of the form (q(1), (q(2))) over bar, s, (s) over bar), where q(1) and q(2) are uor d quarks.

**PHYSICS LETTERS B 833[137335], 2022. DOI:** 10.1016/j.physletb.2022.137335

[P212-2022] "A computational study on the mechanical properties of Pentahexoctite single-layer: Combining DFT and classical molecular dynamics simulations"

Brandao, W. H. S.; Aguiar, A. L.; Ribeiro Junior, L. A.; Galvão, D. S.\*; Sousa, J. M. de\*

Studies aimed at designing new allotropic forms of carbon have received much attention. Recently, a new 2D graphene-like allotrope named Pentahexoctite was theoretically proposed. Pentahexoctite has a metallic signature, and its structure consists of continuous 5-6-8 rings of carbon atoms with sp(2) hybridization. Here, we carried out fully-atomistic computational simulations, combining reactive (ReaxFF) molecular dynamics (MD) and density functional theory (DFT) methods, to study the elastic properties and fracture patterns of Pentahexoctite monolayer. Results revealed a Young's Modulus of 0.74 TPa, smaller than the graphene one (about 1.0 TPa). The Pentahexoctite monolayer, when subjected to a critical strain, goes directly from elastic to completely fractured regimes. This process occurs with no plasticity stages between these two regimes. Importantly, graphene presents a similar fracture process. The elastic properties calculated with both DFT and MD are in good agreement.

**CHEMICAL PHYSICS 563, 111686, 2022. DOI:** 10.1016/j.chemphys.2022.111686

[P213-2022] "A TD-DFT-Based Study on the Attack of the OH center dot Radical on a Guanine Nucleotide"

Santiago, J.\*; Faria, J. C. de; San-Miguel, M.; Bernal, M. A.\*

Heavy charged particles induce severe damage in DNA, which is a radiobiological advantage when treating radioresistant tumors. However, these particles can also induce cancer in humans exposed to them, such as astronauts in space missions. This damage can be directly induced by the radiation or indirectly by the attack of free radicals mainly produced by water radiolysis. We previously studied the impact of a proton on a DNA base pair, using the Time Dependent-Density Functional Theory (TD-DFT).

In this work, we go a step further and study the attack of the OH center dot radical on the Guanine nucleotide to unveil how this molecule subsequently dissociates. The OH center dot attack on the H1 ', H2 ', H3 ', and H5 ' atoms in the guanine was investigated using the Ehrenfest dynamics within the TD-DFT framework. In all cases, the hydrogen abstraction succeeded, and the subsequent base pair dissociation was observed. The DNA dissociates in three major fragments: the phosphate group, the deoxyribose sugar, and the nitrogenous base, with slight differences, no matter which hydrogen atom was attacked. Hydrogen abstraction occurs at about 6 fs, and the nucleotide dissociation at about 100 fs, which agrees with our previous result for the direct proton impact on the DNA. These calculations may be a reference for adjusting reactive force fields so that more complex DNA structures can be studied using classical molecular dynamics, including both direct and indirect DNA damage.

INTERNATIONAL JOURNAL OF MOLECULAR SCIENCES 23[17], 10007, 2022. DOI: 10.3390/ijms231710007

[P214-2022] "Al-enabled photonic smart garment for movement analysis"

Avellar, L.; Stefano Filho, C.\*; Delgado, G.; Frizera, A.; Rocon, E.; Leal Junior, A.

Smart textiles are novel solutions for remote healthcare monitoring which involve non-invasive sensors-integrated clothing. Polymer optical fiber (POF) sensors have attractive features for smart textile technology, and combined with Artificial Intelligence (AI) algorithms increase the potential of intelligent decision-making. This paper presents the development of a fully portable photonic smart garment with 30 multiplexed POF sensors combined with AI algorithms to evaluate the system ability on the activity classification of multiple subjects. Six daily activities are evaluated: standing, sitting, squatting, up-and-down arms, walking and running. A k-nearest neighbors classifier is employed and results from 10 trials of all volunteers presented an accuracy of 94.00 (0.14)%. To achieve an optimal amount of sensors, the principal component analysis is used for one volunteer and results showed an accuracy of 98.14 (0.31)% using 10 sensors, 1.82% lower than using 30 sensors. Cadence and breathing rate were estimated and compared to the data from an inertial measurement unit located on the garment back and the highest error was 2.22%. Shoulder flexion/extension was also evaluated. The proposed approach presented feasibility for activity recognition and movement-related parameters extraction, leading to a system fully optimized, including the number of sensors and wireless communication, for Healthcare 4.0.

SCIENTIFIC REPORTS 12[1], 4067, 2022. DOI: 10.1038/s41598-022-08048-9

[P215-2022] "Amination of Boron-Doped Diamond Surfaces"

Li, C. X.; Oliveira, E. F.\*; Zhang, X.; Biswas, A.; Roy, S.; Puthirath, A. B.; Ruzmetov, D. A.; Neupane, M. R.; Weil, J. D.; Birdwell, G.; Ivanov, T. G.; Terlier, T.; Gray, T.; Kannan, H.; Vajtai, R.; Galvão, D. S.\*; Ajayan, P. M.

Functionalized, especially aminated boron-doped diamond (BDD), is of great interest for catalytic, molecular, and biosensing applications due to its attractive properties. Among various established techniques for diamond amination, UV irradiation in ammonia gas (NH3) has been adopted widely for its simplicity and cost-effectiveness. However, the resultant amination efficiency is found to be relatively low, hindering its usefulness in relevant technologies. In this work, we report a novel strategy for BDD amination by UV irradiation in NH3 that enhances the amination efficiency and results in primary amine dominance. We showed that with hydrobromic acid (HBr) treatment,

the nitrogen concentration increased to greater than 6% on the BDD surface. Importantly, it was found that the partial concentrations of both amine groups (primary -NH2 and secondary =NH) strongly depend on the preoxidation states of hydrogenated BDD (HBDD). HBDD treated with sulfuric and nitric acids (H2SO4/HNO3) presented a primary amine group (-NH2) coverage of approximately 94%, whereas the one modified by piranha solution was approximately 63% after amination. Additionally, with such treatments, the sp(2) carbon cleaning and surface smoothening effects were also observed on the BDD, which provides an alternative to cleaning the diamond surface. Theoretical simulations provided insights into the mechanisms of HBr treatment, stability of nitrogen-related groups, and relative group formation. Our work demonstrates the improved amination efficiency and the dominant amine group coverage on the BDD surface, which will be useful for various applications.

CHEMISTRY OF MATERIALS, 2022. DOI: 10.1021/acs. chemmater.2c00711, Acesso Antecipado: Aug. 2022

[P216-2022] "Arrival Directions of Cosmic Rays above 32 EeV from Phase One of the Pierre Auger Observatory"

Abreu, P.; Aglietta, M.; Arbeletche, L. B.\*; Chinellato, J. A.\*; Oliveira, F. D. de\*; Dobrigkeit, C.\*; Fauth, A. C.\*; Payeras, A. M.\*; Muller, M. A.\*; et al. Pierre Auger Collaboration

A promising energy range to look for angular correlations between cosmic rays of extragalactic origin and their sources is at the highest energies, above a few tens of EeV (1 EeV equivalent to 10(18) eV). Despite the flux of these particles being extremely low, the area of similar to 3000 km(2) covered at the Pierre Auger Observatory, and the 17 yr data-taking period of the Phase 1 of its operations, have enabled us to measure the arrival directions of more than 2600 ultra-high-energy cosmic rays above 32 EeV. We publish this data set, the largest available at such energies from an integrated exposure of 122,000 km(2) sr yr, and search it for anisotropies over the 3.4 pi steradians covered with the Observatory. Evidence for a deviation in excess of isotropy at intermediate angular scales, with similar to 15 degrees Gaussian spread or similar to 25 degrees top-hat radius, is obtained at the 4 sigma significance level for cosmic-ray energies above similar to 40 EeV.

**ASTROPHYSICAL JOURNAL 935[2], 170, 2022. DOI:** 10.3847/1538-4357/ac7d4e

[P217-2022] "Chaotic dynamics of a spinless axisymmetric extended body around a Schwarzschild black hole"

Mosna, R. A.; Rodrigues, F. F.\*; Vieira, R. S. S.

We investigate the long-term orbital dynamics of spinless extended bodies in Schwarzschild geometry, and show that periodic deviations from spherical symmetry in the shape of a test body may trigger the onset of chaos. We do this by applying Dixon's formalism at quadrupolar order to a nearly spherical body whose shape oscillates between a prolate and an oblate spheroid. The late-time chaotic behavior is then verified by applying Melnikov's method.

PHYSICAL REVIEW D 106[2], 024016, 2022. DOI: 10.1103/ PhysRevD.106.024016

[P218-2022] "Dark energy survey year 3 results: cosmological constraints from the analysis of cosmic shear in harmonic space"

Doux, C.; Jain, B.; Alsina, A. N.\*; et al. DES Collaboration

We present cosmological constraints from the analysis of angular power spectra of cosmic shear maps based on data from the first three years of observations by the Dark Energy Survey (DES Y3). Our measurements are based on the pseudo-Ct method and complement the analysis of the two-point correlation functions in real space, as the two estimators are known to compress and select Gaussian information in different ways, due to scale cuts. They may also be differently affected by systematic effects and theoretical uncertainties, making this analysis an important cross-check. Using the same fiducial Lambda cold dark matter model as in the DES Y3 real--space analysis, we find S-8 = sigma(s)(root)Omega m/0.3 =0.7931(-0.025)(+0.038), which further improves to S-8 = 0.784 +/- 0.026 when including shear ratios. This result is within expected statistical fluctuations from the real-space constraint, and in agreement with DES Y3 analyses of non-Gaussian statistics, but favours a slightly higher value of S-8, which reduces the tension with the Planck 2018 constraints from 2.3 sigma in the real space analysis to 1.5 sigma here. We explore less conservative intrinsic alignments models than the one adopted in our fiducial analysis, finding no clear preference for a more complex model. We also include small scales, using an increased Fourier mode cut-off up to k(max) = 5 h Mpc(-1), which allows to constrain baryonic feedback while leaving cosmological constraints essentially unchanged. Finally, we present an approximate reconstruction of the linear matter power spectrum at present time, found to be about 20 per cent lower than predicted by Planck 2018, as reflected by the lower S-8 value.

MONTHLY NOTICES OF THE ROYAL ASTRONOMICAL SOCIETY 515[2], p. 1942-1972, 2022. DOI: 10.1093/mnras/stac1826

[P219-2022] "Disclosing the Biocide Activity of alpha-Ag2--2xCuxWO4 (0 <= x <= 0.16) Solid Solutions"

Pereira, P. F. D. dos; De Foggi, C. C.; Gouveia, A. F.; Pinatti, I. M.; Cabral, L. A.\*; Guillamon, E.; Sorribes, I.; San-Miguel, M. A.; Vergani, C. E.; Simoes, A. Z.; Silva, E. Z. da\*; Cavalcante, L. S.; Llusar, R.; Longo, E.; Andres, J.

In this work, alpha-Ag2-2xCuxWO4 (0 <= x <= 0.16) solid solutions with enhanced antibacterial (against methicillin-resistant Staphylococcus aureus) and antifungal (against Candida albicans) activities are reported. A plethora of techniques (X-ray diffraction with Rietveld refinements, inductively coupled plasma atomic emission spectrometry, micro-Raman spectroscopy, attenuated total reflectance-Fourier transform infrared spectroscopy, field emission scanning electron microscopy, ultraviolet-visible spectroscopy, photoluminescence emissions, and X-ray photoelectron spectroscopy) were employed to characterize the as-synthetized samples and determine the local coordination geometry of Cu2+ cations at the orthorhombic lattice. To find a correlation between morphology and biocide activity, the experimental results were sustained by first-principles calculations at the density functional theory level to decipher the cluster coordinations and electronic properties of the exposed surfaces. Based on the analysis of the under-coordinated Ag and Cu clusters at the (010) and (101) exposed surfaces, we propose a mechanism to explain the biocide activity of these solid solutions.

INTERNATIONAL JOURNAL OF MOLECULAR SCIENCES 23[18], 10589, 2022. DOI: 10.3390/ijms231810589

[P220-2022] "Diversity patterns and speciation processes in a two-island system with continuous migration"

Princepe, D.\*; Czarnobai, S.; Pradella, T. M.\*; Caetano, R. A.; Marquitti, F. M. D.\*; Aguiar, M. A. M. de\*; Araujo, S. B. L.

Geographic isolation is a central mechanism of speciation, but perfect isolation of populations is rare. Although speciation can be hindered if gene flow is large,

intermediate levels of migration can enhance speciation by introducing genetic novelty in the semi-isolated populations or founding small communities of migrants. Here, we consider a two-island neutral model of speciation with continuous migration and study diversity patterns as a function of the migration probability, population size, and number of genes involved in reproductive isolation (dubbed as genome size). For small genomes, low levels of migration induce speciation on the islands that otherwise would not occur. Diversity, however, drops sharply to a single species inhabiting both islands as the migration probability increases. For large genomes, sympatric speciation occurs even when the islands are strictly isolated. Then species richness per island increases with the probability of migration, but the total number of species decreases as they become cosmopolitan. For each genome size, there is an optimal migration intensity for each population size that maximizes the number of species. We discuss the observed modes of speciation induced by migration and how they increase species richness in the insular system while promoting asymmetry between the islands and hindering endemism.

**EVOLUTION, 2022. DOI:** 10.1111/evo.14603, Acesso Antecipado: Sept. 2022

[P221-2022] "Doped Carbon Quantum Dots/PVA Nanocomposite as a Platform to Sense Nitrite Ions in Meat"

Carneiro, S. V.; Oliveira, J. J. P.; Rodrigues, V. S. F.; Fechine, L. M. U. D.; Antunes, R. A.; Alves Neto, M. L.\*; Moura, T. A. de; Cesar, C. L.; Carvalho, H. F. de\*; Paschoal, A. R.; Freire, R. M.; Fechine, P. B. A.

A sensor device based on doped-carbon quantum dots is proposed herein for detection of nitrite in meat products by fluorescence quenching. For the sensing platform, carbon quantum dots doped with boron and functionalized with nitrogen (B,N--Cdot) were synthesized with an excellent 44.3% quantum yield via a one-step hydrothermal route using citric acid, boric acid, and branched polyethylenimine as carbon, boron, and nitrogen sources, respectively. After investigation of their chemical structure and fluorescent properties, the B,N-Cdot at aqueous suspensions showed high selectivity for NO2- in a linear range from 20 to 50 mmol L-1 under optimum conditions at pH 7.4 and a 340 nm excitation. Furthermore, the prepared B,N-Cdots successfully detected NO2- in a real meat sample with recovery of 91.4-104% within the analyzed range. In this manner, a B,N-Cdot/ PVA nanocomposite film with blue emission under excitation at 360 nm was prepared, and a first assay detection of NO2- in meat products was tested using a smartphone application. The potential application of the newly developed sensing device containing a highly fluorescent probe should aid in the development of a rapid and inexpensive strategy for NO2- detection.

ACS APPLIED MATERIALS & INTERFACES, 2022. DOI: 10.1021/acsami.2c09197, Acesso Antecipado: Sept. 2022

[P222-2022] "Exploring the N Lambda-N Sigma coupled system with high precision correlation techniques at the LHC"

Acharya, S.; Adamova, D.; Chinellato, D. D.\*; Guardiano, G. G.\*; Jahnke, C.\*; Takahashi, J.\*; et al. ALICE Collaboration

The interaction of Lambda and Sigma hyperons (Y) with nucleons (N) is strongly influenced by the coupled-channel dynamics. Due to the small mass difference of the N Lambda and N Sigma systems, the sizable coupling strength of the N Sigma <-> N Lambda processes constitutes a crucial element in the determination of the N Lambda interaction. In this letter we present the most precise measurements on the interaction of p Lambda pairs, from zero relative momentum up to the opening of the N Sigma channel.

The correlation function in the relative momentum space for p Lambda circle plus (p) over bar(Lambda) over bar pairs measured in high-multiplicity triggered pp collisions at root s = 13TeV at the LHC is reported. The opening of the inelastic N Sigma channels is visible in the extracted correlation function as a cusp-like structure occurring at relative momentum k\* = 289 MeV/c. This represents the first direct experimental observation of the N Sigma <-> N Lambda coupled channel in the p Lambda system. The correlation function is compared with recent chiral effective field theory calculations, based on different strengths of the N Sigma <-> N Lambda transition potential. A weaker coupling, as possibly supported by the present measurement, would require a more repulsive three-body NN Lambda interaction for a proper description of the Lambda in-medium properties, which has implications on the nuclear equation of state and for the presence of hyperons inside neutron stars.

PHYSICS LETTERS B 833, 137272, 2022. DOI: 10.1016/j.physletb.2022.137272

[P223-2022] "Extinction and hybridization in a neutral model of speciation"

Botelho, L. L.\*; Marquitti, F. M. D.\*; Aguiar, M. A. M. de\*

Evolution is usually pictured as a tree where ancient species branch into new ones and eventually disappear. In this simplified view, the balance between speciation and extinction fully determines the diversity of life. Hybridization, however, introduces another level of complexity, allowing neighboring branches of the tree to interact, mixing their genetic content. This generates further diversity leading to reticulated trees. In this paper we study processes of speciation, extinction and hybridization using a genetically and spatially explicit neutral model of diversification. The model is based on the Derrida--Higgs formulation, where the genome of haploid individuals is represented by binary strings and reproduction is constrained by genetic similarity. Tracking all events of speciation, extinction and hybridization throughout the evolutionary process allows us to compute complete and exact phylogenetic trees. We found that genome size played a key role in these processes, increasing the extinction rate and decreasing the hybridization rate. Only in the limit of large genomes the simplified picture of a branching tree is recovered. Most hybridization events occurred between relatively abundant species, discarding lack of sexual partners or small population sizes as potential causes. We found that hybridization occurred mostly because of opportunity (genetic similarity and spatial proximity) between recently branched species, when the number of accumulated mutations is not yet too large.

JOURNAL OF PHYSICS A-MATHEMATICAL AND THEORETICAL 55[38], 385601, 2022. DOI: 10.1088/1751-8121/ac88a5

[P224-2022] "High throughput investigation of an emergent and naturally abundant 2D material: Clinochlore"

Oliveira, R. de; Guallichico, L. A. G.; Policarpo, E.; Cadore, A. R.; Freitas, R. O.; Silva, F. M. C. da\*; Teixeira, V. de C.; Paniago, R. M.; Chacham, H.; Matos, M. J. S.; Malachias, A.; Krambrock, K.; Barcelos, I. D.

Phyllosilicate minerals, which form a class of naturally occurring layered materials (LMs), have been recently considered as a low-cost source of two-dimensional (2D) materials. Clinochlore [Mg5Al(AlSi3)O-10(OH)(8)] is one of the most abundant phyllosilicate minerals in nature, exhibiting the capability to be mechanically exfoliated down to a few layers. An important characteristic of clinochlore is the natural occurrence of defects and impurities which can strongly affect their optoelectronic properties, possibly in technologically interesting ways.

In the present work, we carry out a thorough investigation of the clinochlore structure on both bulk and 2D exfoliated forms, discussing its optical features and the influence of the insertion of impurities on its macroscopic properties. Several experimental techniques are employed, followed by theoretical first-principles calculations considering several types of naturally-ocurring transition metal impurities in the mineral lattice and their effect on electronic and optical properties. We demonstrate the existence of requirements concerning surface quality and insulating properties of clinochlore that are mandatory for its suitable application in nanoelectronic devices. The results presented in this work provide important informations for clinochlore potential applications and establish a basis for further works that intend to optimize its properties to relevant 2D technological applications through defect engineering.

**APPLIED SURFACE SCIENCE 599, 153959, 2022. DOI:** 10.1016/j.apsusc.2022.153959

[P225-2022] "Inclusive nonresonant multilepton probes of new phenomena at root s=13 TeV"

Tumasyan, A.; Adam, W.; Chinellato, J. A.\*; et al. CMS Collaboration

An inclusive search for nonresonant signatures of beyond the standard model (SM) phenomena in events with three or more charged leptons, including hadronically decaying tau leptons, is presented. The analysis is based on a data sample corresponding to an integrated luminosity of 138 fb(-1) of proton-proton collisions at root s = 13 TeV, collected by the CMS experiment at the LHC in 2016-2018. Events are categorized based on the lepton and b-tagged jet multiplicities and various kinematic variables. Three scenarios of physics beyond the SM are probed, and signal-specific boosted decision trees are used for enhancing sensitivity. No significant deviations from the background expectations are observed. Lower limits are set at 95% confidence level on the mass of type-III seesaw heavy fermions in the range 845-1065 GeV for various decay branching fraction combinations to SM leptons. Doublet and singlet vectorlike tau lepton extensions of the SM are excluded for masses below 1045 GeV and in the mass range 125-150 GeV, respectively. Scalar leptoquarks decaying exclusively to a top quark and a lepton are excluded below 1.12-1.42 TeV, depending on the lepton flavor. For the type-III seesaw as well as the vectorlike doublet model, these constraints are the most stringent to date. For the vectorlike singlet model, these are the first constraints from the LHC experiments. Detailed results are also presented to facilitate alternative theoretical interpretations.

PHYSICAL REVIEW D 105[11], 112007, 2022. DOI: 10.1103/ PhysRevD.105.112007

[P226-2022] "Kraft lignin-based carbon xerogel/zinc oxide composite for 4-chlorophenol solar-light photocatalytic degradation: effect of pH, salinity, and simultaneous Cr(VI) reduction"

Moraes, N. P. de; Siervo, A. de\*; Silva, T. O.; Rocha, R. D.; Reddy, D. A.; Yu, L. Q.; Lanza, M. R. D. de; Rodrigues, L. A.

Considering the ever-increasing need for efficient wastewater treatment, this study focused on the development of new kraft lignin-based carbon xerogel/zinc oxide (XCL/ZnO w) photocatalysts. The inclusion of the carbon xerogel is expected to cause an improvement in charge transfer throughout the photoactivation process, consequently enhancing its overall photocatalytic efficiency. Characterization shows that the materials developed are composed of both zinc oxide and carbon xerogel. The addition of the lignin-based carbon xerogel caused a significant morphological modification to the composite materials, resulting in a greater specific surface area.

Regarding the photocatalytic efficiency, the optimized composite (XCL/ZnO 1.0) displayed superior efficiency to the pure zinc oxide, especially when calcined at 700 degrees C, with an increase of 20% in the overall photodegradation capacity for the 4-chlorophenol (4CP) molecule. The XCL/ZnO 1.0 also displayed better performance than its tannin counterpart, previously reported in the literature, obtaining a 60% increase in the apparent reaction rate constant. The XCL/ZnO 1.0 also displayed better performance for the simultaneous hexavalent chrome (Cr (VI)) reduction/4CP oxidation reaction. Salinity and system pH had a significant influence on the efficiency of the 4CP photodegradation, as higher values of salinity and lower pHs caused a decrease in the overall efficiency of the process. At last, chronoamperometry and open-circuit potential tests confirmed the superiority of the XCL/ZnO 1.0 over the pure ZnO, highlighting the beneficial impact of the carbon xerogel on the charge transport dynamics of the composite.

ENVIRONMENTAL SCIENCE AND POLLUTION RESEARCH, 2022. DOI: 10.1007/s11356-022-22825-z, Acesso Antecipado: Sept. 2022

[P227-2022] "Manganese silicide nanowires via metallic flux nanonucleation: growth mechanism and temperature-dependent resistivity"

Cruz, A. S. E.\*; Campanelli, R. B.\*; Santos, M. V. P. dos\*; Fabris, F.\*; Bettini, J.; Pagliuso, P. G.\*; Pirota, K. R.\*

Mn5Si3 nanowires are believed to be the building blocks of the newest trends of flexible and stretchable devices in nanoelectronics. In this context, growing Mn5Si3 nanowires, as well as characterizing their electronic transport properties provide insight into their phenomenology. In this work, we report on the growth mechanism of Mn5Si3 nanowires produced by the metallic flux nanonucleation method, as well as the resistivity measurements of these nanostructures. Our calculation allows us, by using the Washburn equation for pore infiltration, to give a guess on why we obtain Mn-rich nanowires. In addition, some morphological aspects of the diameter-modulated Mn5Si3 nanowires were discussed based on the classical nucleation theory. From the resistivity measurements for the smallest diameter among the nanowires, we observed a significant reduction of around 37% of the phonons characteristic temperature by fitting the Bloch-Grunesein formula with other sources of scattering. Our results lead to a better understanding on the recent metallic flux nanonucleation growth method, as well as going a step further into the electronic transport properties of the Mn5Si3 nanowires.

**NANOTECHNOLOGY 33[47], 475704, 2022. DOI:** 10.1088/1361-6528/ac893c

[P228-2022] "Measurement of the Drell-Yan forward-backward asymmetry at high dilepton masses in proton-proton collisions at root s=13 TeV"

Tumasyan, A.; Adam, W.; Chinellato, J. A.\*; et al. CMS Collaboration

A measurement of the forward-backward asymmetry of pairs of oppositely charged leptons (dimuons and dielectrons) produced by the Drell-Yan process in proton-proton collisions is presented. The data sample corresponds to an integrated luminosity of 138 fb(-1) collected with the CMS detector at the LHC at a center-of-mass energy of 13 TeV. The asymmetry is measured as a function of lepton pair mass for masses larger than 170 GeV and compared with standard model predictions. An inclusive measurement across both channels and the full mass range yields an asymmetry of 0.612 +/- 0.005 (stat) +/- 0.007 (syst). As a test of lepton flavor universality, the difference between the dimuon and dielectron asymmetries is measured as well.

No statistically significant deviations from standard model predictions are observed. The measurements are used to set limits on the presence of additional gauge bosons. For a Z' boson in the sequential standard model the observed (expected) 95% confidence level lower limit on the Z' mass is 4.4 TeV (3.7 TeV).

JOURNAL OF HIGH ENERGY PHYSICS [8], 063, 2022. DOI: 10.1007/JHEP08(2022)063

[P229-2022] "Mechanical properties of 3D-printed penta-diamond"

Felix, L. C.\*; Ambekar, R. S.; Woellner, C. F.; Kushwaha, B.; Pal, V.; Tiwary, C. S.; Galvão, D. S.\*

In this work, we combined fully atomistic molecular dynamics and finite elements simulations with mechanical testings to investigate the mechanical behavior of atomic and 3D-printed models of pentadiamond. Pentadiamond is a recently proposed new carbon allotrope, which is composed of a covalent network of pentagonal rings. Our results showed that the stress-strain (SS) behavior is almost scale-independent. The SS curves of the 3D-printed structures exhibit three characteristic regions. For low-strain values, this first region presents a non-linear behavior close to zero, followed by a well-defined linear behavior. The second regime is a quasi-plastic one and the third one is densification followed by structural failures (fracture). Young's modulus values decrease from 520 to 486 MPa. The deformation mechanism is bending-dominated and different from the layer-by-layer deformation mechanism observed for other 3D--printed structures. They exhibit good energy absorption capabilities (3.5 MJ kg(-1)), with some structures even outperforming epoxy Kevlar and TRIP-steel. The structures show better absorption potential than the well-known porous architectures such as honeycomb, schwarzites, and tubulanes and occupy the same region of woven structures in the Ashby chart.

JOURNAL OF PHYSICS D-APPLIED PHYSICS 55[46], 465301, 2022. DOI: 10.1088/1361-6463/ac91dc

[P230-2022] "Modeling functional network topology following stroke through graph theory: functional reorganization and motor recovery prediction"

Almeida, S. R. M.; Stefano Filho, C. A.\*; Vicentini, J.; Novi, S. L.\*; Mesquita, R. C.\*; Castellano, G.\*; Li, L. M.

The study of functional reorganization following stroke has been steadily growing supported by advances in neuroimaging techniques, such as functional magnetic resonance imaging (fMRI). Concomitantly, graph theory has been increasingly employed in neuroscience to model the brain's functional connectivity (FC) and to investigate it in a variety of contexts. The aims of this study were: 1) to investigate the reorganization of network topology in the ipsilesional (IL) and contralesional (CL) hemispheres of stroke patients with (motor stroke group) and without (control stroke group) motor impairment, and 2) to predict motor recovery through the relationship between local topological variations of the functional network and increased motor function. We modeled the brain's FC as a graph using fMRI data, and we characterized its interactions with the following graph metrics: degree, clustering coefficient, characteristic path length, and betweenness centrality (BC). For both patient groups, BC yielded the largest variations between the two analyzed time points, especially in the motor stroke group. This group presented significant correlations (P <0.05) between average BC changes and the improvements in upper-extremity Fugl-Meyer (UE-FM) scores at the primary sensorimotor cortex and the supplementary motor area for the CL hemisphere. These regions participate in processes related to the selection, planning, and execution of movement.

Generally, higher increases in average BC over these areas were related to larger improvements in UE-FM assessment. Although the sample was small, these results suggest the possibility of using BC as an indication of brain plasticity mechanisms following stroke.

BRAZILIAN JOURNAL OF MEDICAL AND BIOLOGICAL RESEAR-CH 55[1], e12036, 2022. DOI: 10.1590/1414-431X2022e12036

[P231-2022] "Nuclear transverse momentum broadening in the color dipole approach at the LHC regime"

Ben, F. G.; Giannini, A. V.\*; Machado, M. V. T.

Transverse momentum broadening of a parton propagating through a large nucleus is evaluated in the color dipole approach using different models for the dipole cross section or unintegrated gluon distribution, which lead to different values of the coefficient C-F(0, s). Numerical calculations are compared to data extracted from LHCb, ALICE and PHENIX experiments for the nuclear broadening of J/psi mesons. We find that different models which describe the small-x data predict values of nuclear broadening of transverse momentum that agree reasonably well with experiment. The centrality dependence was also analysed and the models are consistent with the ALICE measurements. Available experimental results, however, are not able to clearly distinguish the performance of the considered models.

JOURNAL OF PHYSICS G-NUCLEAR AND PARTICLE PHYSICS 49[10], 105005, 2022. DOI: 10.1088/1361-6471/ac8b27

[P232-2022] "Observation of B-0 ->psi(2S)K-S(0)pi(+)pi(-) and B-s(0)->psi(2S)K-S(0) decays"

Tumasyan, A.; Adam, W.; Chinellato, J. A.\*; et al. CMS Collaboration

Using a data sample of root s = 13 TeV protonproton collisions collected by the CMS experiment at the LHC in 2017 and 2018 with an integrated luminosity of 103 fb(-1), the B-s(0) -> psi(2S) K-S(0) and B-0 -> psi(2S)K-S(0) pi(+) pi(-) decays are observed with significances exceeding 5 standard deviations. The resulting branching fraction ratios, measured for the first time, correspond to B(B-s(0) -> psi(2S)K-S(0))/B(B-0 Zeta -> psi(2S)K-S(0)) =  $(3.33 + -0.69(\text{stat}) + -0.11 (\text{syst}) + -0.34 (\text{f(s)}/\text{f(d)})) \times 10(-2)$  and B(B-0 -> psi(2S)K-S(0) pi(+) pi(-))/B(B-0 -> psi(2S)K-S(0)) = 0.480 + -0.013 (stat) + -0.032 (syst), where the last uncertainty in the first ratio is related to the uncertainty in the ratio of production cross sections of B-s(0) and B-0 mesons, f(s)/f(d).

**EUROPEAN PHYSICAL JOURNAL C 82[5], 499, 2022. DOI:** 10.1140/epjc/s10052-022-10315-y

[P233-2022] "Optical fiber specklegram sensor for multi--point curvature measurements"

Fujiwara, E.; Cabral, T. D.\*

We present a multi-point curvature sensor based on optical fiber specklegram measurements. Apart from the current approaches, the proposed system uses an ordinary multimode fiber excited with visible light as a reflection-type probe. Besides, this method discretizes the waveguide into segments connected by joints and assumes sequential bend events, simplifying the specklegram referencing for correlation analyses and avoiding laborious deep learning processing. Sensor characterization yielded a linear response with similar to 1.3 degrees resolution for single curvatures,

whereas shape prediction experiments in the plane resulted in maximum errors of similar to 3.5 degrees and similar to 5.4 mm for angular and linear positioning, respectively. Furthermore, exploratory tests indicated errors < 2.3 degrees regarding probe curvatures in the space. This research introduces a feasible, straightforward alternative to the available shape sensors, enabling applications in medical probes and soft robotics.

APPLIED OPTICS 61[23], p. 6787-6794, 2022. DOI: 10.1364/AO.464503

[P234-2022] "Optical imaging and spectroscopy for the study of the human brain: status report"

Ayaz, H.; Baker, W. B.; Mesquita, R. C.\*; Novi, S. L.\*; et al.

This report is the second part of a comprehensive two-part series aimed at reviewing an extensive and diverse toolkit of novel methods to explore brain health and function. While the first report focused on neurophotonic tools mostly applicable to animal studies, here, we highlight optical spectroscopy and imaging methods relevant to noninvasive human brain studies. We outline current state-of-the-art technologies and software advances, explore the most recent impact of these technologies on neuroscience and clinical applications, identify the areas where innovation is needed, and provide an outlook for the future directions.

**NEUROPHOTONICS 9, Supl. 2, 2022. DOI:** 10.1117/1.NPh.9.S2. S24001

[P235-2022] "Optimal finite-time processes in weakly driven overdamped Brownian motion"

Naze, P.\*; Deffner, S.\*; Bonanca, M. V. S.\*

The complete physical understanding of the optimization of the thermodynamic work still is an important open problem in stochastic thermodynamics. We address this issue using the Hamiltonian approach of linear response theory in finite time and weak processes. We derive the Euler-Lagrange equation associated and discuss its main features, illustrating them using the paradigmatic example of driven Brownian motion in overdamped regime. We show that the optimal protocols obtained either coincide, in the appropriate limit, with the exact solutions by stochastic thermodynamics or can be even identical to them, presenting the well-known jumps. However, our approach reveals that jumps at the extremities of the process are a good optimization strategy in the regime of fast but weak processes for any driven system. Additionally, we show that fast-but-weak optimal protocols are time-reversal symmetric, a property that has until now remained hidden in the exact solutions far from equilibrium.

JOURNAL OF PHYSICS COMMUNICATIONS 6[8], 083001, 2022. DOI: 10.1088/2399-6528/ac871d

[P236-2022] "Optimization of image quality and dose in adult and pediatric chest radiography via Monte Carlo simulation and experimental methods"

Mendes, H. R.\*; Silva, J. C.\*; Marcondes, M.\*; Tomal, A.\*

Optimization in radiography aims to achieve adequate image quality to enable diagnosis by adjusting the dose to the patient. The figure of merit (FOM) is a well-known optimization method that balances image quality (IQ) and Dose. However, different authors use distinct definitions. This work aims to compare several FOM definitions to determine the most adequate for chest radiography optimization via Monte Carlo (MC) simulation.

Moreover, this study aims to perform a systematic study, evaluating the influence of tube potential, additional filtration, detector technologies, antiscatter grids, and phantom thickness on FOM. The dose was evaluated by the mean absorbed dose (MAD), the entrance skin dose (ESD), and the effective dose (E). The signal-to-noise ratio (SNR) and the contrast-to-noise ratio (CNR) were the IQ indexes. FOM was calculated as IQ2/Dose. Two types of antiscatter grids were simulated. One grid had cotton fiber as an interspace material, and the other grid had aluminum. The simulated detectors were composed of CsI and a-Se, used in digital radiography (DR), and BaFBr, used in computed radiography (CR). The results showed that tube potentials close to 120 kV optimized the SNR for all cases of phantom thickness, dosimetric quantities, and additional filtrations. On the other hand, the op-timum tube potentials for CNR are dependent on these parameters. It was shown that optimizing the CNR provides better overall image quality. Additionally, MAD and E are suitable for optimization studies based on FOM. Additional filtration showed a better dose reduction, with 1 mm Cu having the best performance. Considering both optimization and clinical applicability, additional filters of 0.2 mm Cu + 2 mm Al are indicated. The optimum tube potentials are similar for all antiscatter girds evaluated. When different detectors are applied, the one with a higher effective atomic number provides larger FOM values and optimum tube potential. Experimental validation was performed only with the CR detector due to limitations in the detection technologies available. The dependency of FOM on the tube potential was slightly different between the experimental and MC simulation cases; however, there was an intersection between the optimum tube potential range for both cases. The results in this study yielded a general overview of optimization, analyzing several parameters, providing an improvement in other optimization studies that were limited by either one FOM definition or experimental factors such as one detector and/or one antiscatter grid configuration.

RADIATION PHYSICS AND CHEMISTRY 201, 110396, 2022. DOI: 10.1016/j.radphyschem.2022.110396

[P237-2022] "Performance analysis of continuous-variable quantum key distribution using non-Gaussian states"

Aguiar, L. S.\*; Borelli, L. F. M.\*; Roversi, J. A.\*; Vidiella-Barranco, A.\*

In this study, we analyse the efficiency of a protocol with discrete modulation of continuous variable non-Gaussian states, that is, the coherent states having the addition of one photon followed by the subtraction of one photon (PASCS). We calculate lower bounds of the asymptotic key rates against Gaussian collective attacks based on the fact that for sufficiently small modulation variances we remain close to the protocol with Gaussian modulation. We compare the results of a four-state protocol (quadrature phase-shift-keying) using PASCS with the ones using coherent states, and show that under the same environmental conditions, the former always outperforms the latter, allowing to increase the maximum possible distance for secret key generation. Interestingly, we find that for the protocol using discrete-modulated PASCS, the noisier the line, the better will be its performance compared to the protocol using coherent states, showing that continuous variable non--Gaussian states can be considerably more advantageous for performing quantum key distribution in non-ideal situations.

QUANTUM INFORMATION PROCESSING 21[8], 304, 2022. DOI: 10.1007/s11128-022-03645-z

[P238-2022] "Search for a W' boson decaying to a vector-like quark and a top or bottom quark in the all-jets final state at root s=13 TeV"

Tumasyan, A.; Adam, W.; Chinellato, J. A.\*; et al. CMS Collaboration

A search is presented for a heavy W' boson resonance decaying to a B or T vector-like quark and a t or a b quark, respectively. The analysis is performed using protonproton collisions collected with the CMS detector at the LHC. The data correspond to an integrated luminosity of 138 fb(-1) at a center-of-mass energy of 13 TeV. Both decay channels result in a signature with a t quark, a Higgs or Z boson, and a b quark, each produced with a significant Lorentz boost. The all-hadronic decays of the Higgs or Z boson and of the t quark are selected using jet substructure techniques to reduce standard model backgrounds, resulting in a distinct three-jet W boson decay signature. No significant deviation in data with respect to the standard model background prediction is observed. Upper limits are set at 95% confidence level on the product of the W' boson cross section and the final state branching fraction. A W boson with a mass below 3.1 TeV is excluded, given the benchmark model assumption of democratic branching fractions. In addition, limits are set based on generalizations of these assumptions. These are the most sensitive limits to date for this final state.

JOURNAL OF HIGH ENERGY PHYSICS [9], 088, 2022. DOI: 10.1007/JHEP09(2022)088

[P239-2022] "Search for Flavor-Changing Neutral Current Interactions of the Top Quark and Higgs Boson in Final States with Two Photons in Proton-Proton Collisions at root s=13 TeV"

Tumasyan, A.; Adam, W.; Chinellato, J. A.\*; et al. CMS Collaboration

Proton-proton interactions resulting in final states with two photons are studied in a search for the signature of flavor-changing neutral current interactions of top quarks (t) and Higgs bosons (H). The analysis is based on data collected at a center-of-mass energy of 13 TeV with the CMS detector at the LHC, corresponding to an integrated luminosity of 137 fb(-1.) No significant excess above the background prediction is observed. Upper limits on the branching fractions (B) of the top quark decaying to a Higgs boson and an up (u) or charm (c) quark are derived through a binned fit to the diphoton invariant mass spectrum. The observed (expected) 95% confidence level upper limits are found to be 0.019% (0.031%) for B(t -> Hu) and 0.073% (0.051%) for B(t -> Hc). These are the strictest upper limits yet determined.

PHYSICAL REVIEW LETTERS 129[3], 032001, 2022. DOI: 10.1103/PhysRevLett.129.032001

[P240-2022] "Search for high-mass resonances decaying to a jet and a Lorentz-boosted resonance in proton-proton collisions at root s=13 TeV"

Tumasyan, A.; Adam, W.; Chinellato, J. A.\*; et al. CMS Collaboration

A search is reported for high-mass hadronic resonances that decay to a parton and a Lorentz-boosted resonance, which in turn decays into a pair of partons. The search is based on data collected with the CMS detector at the LHC in proton-proton collisions at root s = 13 TeV, corresponding to an integrated luminosity of 138 fb(-1). The boosted resonance is reconstructed as a single wide jet with substructure consistent with a two-body decay. The high-mass resonance is thus considered as a dijet system. The jet substructure information and the kinematic properties of cascade resonance decays are exploited to disentangle the signal from the large quantum chromodynamics multijet background. The dijet mass spectrum is analyzed for the presence of new high-mass resonances, and is found to be consistent with the standard model background predictions.

Results are interpreted in a warped extra dimension model where the high-mass resonance is a Kaluza-Klein gluon, the boosted resonance is a radion, and the final state partons are all gluons. Limits on the production cross section are set as a function of the Kaluza-Klein gluon and radion masses. These limits exclude at 95% confidence level models with Kaluza-Klein gluon masses in the range 2.0 to 4.3 TeV and radion masses in the range 0.20 to 0.74TeV. By exploring a novel experimental signature, the observed limits on the Kaluza-Klein gluon mass are extended by up to about 1 TeV compared to previous searches.

PHYSICS LETTERS B 832, 137263, 2022. DOI: 10.1016/j.physletb.2022.137263

[P241-2022] "Search for resonances decaying to three W bosons in the hadronic final state in proton-proton collisions at root s=13 TeV"

Tumasyan, A.; Adam, W.; Chinellato, J. A.\*; et al. CMS Collaboration

A search for Kaluza-Klein excited vector boson resonances, WKK, decaying in cascade to three W bosons via a scalar radion R, WKK??? WR??? WWW, in a final state containing two or three massive jets is presented. The search is performed with ffis ffi p = 13 TeV proton-proton collision data collected by the CMS Two final states are simultaneously probed, one where the two W bosons produced by the R decay are reconstructed as separate, large-radius, massive jets, and one where they are merged into a single largeradius jet. The observed data are in agreement with the standard model expectations. Limits are set on the product of the WKK resonance cross section and branching fraction to three W bosons in an extended warped extradimensional model and are the first of their kind at the LHC.

PHYSICAL REVIEW D 106[1], 012002, 2022. DOI: 10.1103/ PhysRevD.106.012002

[P242-2022] "Search for Spatial Correlations of Neutrinos with Ultra-high-energy Cosmic Rays"

Albert, A.; Alves, S.; Arbeletche, L. B.\*; Chinellato, J. A.\*; Oliveira, F. D. de\*; Dobrigkeit, C.\*; Fauth, A. C.\*; Payeras, A. M.\*; Muller, M. A.\*; et al. P IceCube Collaboration; IceCube Collaboration; Pierre Auger Collaboration; Telescope Array Collaboration

For several decades, the origin of ultra-high-energy cosmic rays (UHECRs) has been an unsolved question of high-energy astrophysics. One approach for solving this puzzle is to correlate UHECRs with high-energy neutrinos, since neutrinos are a direct probe of hadronic interactions of cosmic rays and are not deflected by magnetic fields. In this paper, we present three different approaches for correlating the arrival directions of neutrinos with the arrival directions of UHECRs. The neutrino data are provided by the IceCube Neutrino Observatory and ANTARES, while the UHECR data with energies above similar to 50 EeV are provided by the Pierre Auger Observatory and the Telescope Array. All experiments provide increased statistics and improved reconstructions with respect to our previous results reported in 2015. The first analysis uses a high-statistics neutrino sample optimized for point-source searches to search for excesses of neutrino clustering in the vicinity of UHECR directions. The second analysis searches for an excess of UHECRs in the direction of the highest--energy neutrinos. The third analysis searches for an excess of pairs of UHECRs and highest-energy neutrinos on different angular scales. None of the analyses have found a significant excess, and previously reported overfluctuations are reduced in significance. Based on these results, we further constrain the neutrino flux spatially correlated with UHECRs.

**ASTROPHYSICAL JOURNAL 934[2], 164, 2022. DOI:** 10.3847/1538-4357/ac6def

[P243-2022] "Sequential time-window learning with approximate Bayesian computation: an application to epidemic forecasting"

Valeriano, J. P.; Cintra, P. H.\*; Libotte, G.; Reis, I.; Fontinele, F.; Silva, R.; Malta, S.

The long duration of the COVID-19 pandemic allowed for multiple bursts in the infection and death rates, the so-called epidemic waves. This complex behavior is no longer tractable by simple compartmental model and requires more sophisticated mathematical techniques for analyzing epidemic data and generating reliable forecasts. In this work, we propose a framework for analyzing complex dynamical systems by dividing the data in consecutive time-windows to be separately analyzed. We fit parameters for each time-window through an approximate Bayesian computation (ABC) algorithm, and the posterior distribution of parameters obtained for one window is used as the prior distribution for the next window. This Bayesian learning approach is tested with data on CO-VID-19 cases in multiple countries and is shown to improve ABC performance and to produce good short-term forecasting.

NONLINEAR DYNAMICS, 2022. DOI: 10.1007/s11071-022-07865-x, Acesso Antecipado: Sept. 2022

[P244-2022] "Study of very forward energy and its correlation with particle production at midrapidity in pp and p-Pb collisions at the LHC"

Acharya, S.; Adamova, D.; Chinellato, D. D.\*; Guardiano, G. G.\*; Jahnke, C.\*; Takahashi, J.\*; et al. ALICE Collaboration

The energy deposited at very forward rapidities (very forward energy) is a powerful tool for characterising proton fragmentation in pp and p-Pb collisions. The correlation of very forward energy with particle production at midrapidity provides direct insights into the initial stages and the subsequent evolution of the collision. Furthermore, the correlation with the production of particles with large transverse momenta at midrapidity provides information complementary to the measurements of the underlying event, which are usually interpreted in the framework of models implementing centrality--dependent multiple parton interactions. Results about very forward energy, measured by the ALICE zero degree calorimeters (ZDCs), and its dependence on the activity measured at midrapidity in pp collisions at root s = 13 TeV and in p-Pb collisions at root s(NN) = 8.16 TeV are discussed. The measurements performed in pp collisions are compared with the expectations of three hadronic interaction event generators: PYTHIA 6 (Perugia 2011 tune), PYTHIA 8 (Monash tune), and EPOS LHC. These results provide new constraints on the validity of models in describing the beam remnants at very forward rapidities, where perturbative QCD cannot be used.

JOURNAL OF HIGH ENERGY PHYSICS [8], 086, 2022. DOI: 10.1007/JHEP08(2022)086

[P245-2022] "Synthesis of Carbon Nanodots from Sugarcane Syrup, and Their Incorporation into a Hydrogel-Based Composite to Fabricate Innovative Fluorescent Microstructured Polymer Optical Fibers "

Perli, G.; Soares, M. C. P.; Cabral, T. D.\*; Bertuzzi, D. L.; Bartoli, J. R.; Livi, S.; Duchet-Rumeau, J.; Cordeiro, C. M. B.\*; Fujiwara, E.; Ornelas, C.

Carbon nanodots (CNDs) are interesting materials due to their intrinsic fluorescence, electron-transfer properties, and low toxicity. Here, we report a sustainable, cheap, and scalable methodology to obtain CNDs from sugarcane syrup using a domestic microwave oven. The CNDs were characterized by infrared spectroscopy, dynamic light scattering, atomic force microscopy, absorption, and emission spectroscopies. The CNDs have 3 nm in diameter with low polydispersity and are fluorescent. A fluorescent hydrogel-CNDs composite was obtained using gelatin polypeptide as the polymeric matrix. The new hydrogel-CNDs composite was incorporated in the cavities of a double-clad optical fiber using an innovative approach that resulted in a microstructured polymer optical fiber with intrinsic fluorescence. This work shows a promising alternative for the fabrication of fluorescent materials since the CNDs synthesis is sustainable and environmentally friendly. These CNDs might substitute the rare-earth and other heavy metals of high cost and toxicity, which are usually incorporated in double-clad fibers for applications on lasers, amplifiers, and spectroscopy.

GELS 8[9], 553, 2022. DOI: 10.3390/gels8090553

[P246-2022] "The Double Chooz antineutrino detectors"

Kerret, H. de; Abe, Y.; Gonzalez, L. F. G.\*; Kemp, E.\*; et al.

This article describes the setup and performance of the near and far detectors in the Double Chooz experiment. The electron antineutrinos of the Chooz nuclear power plant were measured in two identically designed detectors with different average baselines of about 400 m and 1050 m from the two reactor cores. Over many years of data taking the neutrino signals were extracted from interactions in the detectors with the goal of measuring a fundamental parameter in the context of neutrino oscillation, the mixing angle 013. The central part of the Double Chooz detectors was a main detector comprising four cylindrical volumes filled with organic liquids. From the inside towards the outside there were volumes con-taining gadolinium-loaded scintillator, gadolinium-free scintillator, a buffer oil and, optically separated, another liquid scintillator acting as veto system. Above this main detector an additional outer veto system using plastic scintillator strips was installed. The technologies developed in Double Chooz were inspiration for several other antineutrino detectors in the field. The detector design allowed implementation of efficient background rejection techniques including use of pulse shape information provided by the data acquisition system. The Double Chooz detectors featured remarkable stability, in particular for the detected photons, as well as high radiopurity of the detector components.

**EUROPEAN PHYSICAL JOURNAL C 82[9], 804, 2022. DOI:** 10.1140/epjc/s10052-022-10726-x

[P247-2022] "Transport coefficients of quasiparticle models within a new relaxation time approximation of the Boltzmann equation"

Rocha, G. S.; Ferreira, M. N.\*; Denicol, G. S.; Noronha, J.

We investigate the transport properties of a kinetic theory model that is tuned to describe the thermodynamic properties of QCD at zero chemical potential using a new formulation of the relaxation time approximation. In contrast to previous approaches, the latter is constructed to preserve the fundamental properties of the collision term of the Boltzmann equation for any energy dependence of the relaxation time. A novel choice of matching conditions is implemented to ensure that the background mean-field depends only on the temperature even when the system is out of equilibrium. We provide a consistent analysis of how the transport coefficients of relativistic Navier-Stokes theory vary with the energy dependence of the relaxation time.

We also show that the entropy production of this theory is consistent with the second law of thermodynamics and verify that it is independent of the matching conditions employed. We used this fact to calculate the matching independent combination of transport coefficients.

PHYSICAL REVIEW D 106[3], 036022, 2022. DOI: 10.1103/ PhysRevD.106.036022

[P248-2022] "Valence State Tuning of Gold Nanoparticles in the Dewetting Process: An X-ray Photoelectron Spectroscopy Study"

Lanza, G. S. V.; Jimenez, M. J. M.; Alvarez, F.\*; Perez-Taborda, J. A.; Avila, A.

Gold nanoparticles (AuNPs) are commonly synthesized using the citrate reduction method, reducing Au3+ into Au1+ ions and facilitating the disproportionation of aurous species to Au atoms (Au-0). This method results on citrate-capped AuNPs with valence single states Au-0. Here, we report a methodology that allows obtaining AuNPs by the dewetting process with three different valence states (Au3+, Au1+, and Au-0), which can be fine-tuned with ion bombardment. The chemical surface changes and binding state of the NPs were investigated using core-level X-ray photoelectron spectroscopy (XPS). This is achieved by recording high-resolution Au 4f XPS spectra as a function of ion dose exposure. The results obtained show a time-dependent tuning effect on the Au valence states using low-energy 200 V acceleration voltage Ar+ ion bombardment, and the valence state conversion kinetics involves the reduction from Au3+ and Au1+ to Au-0. Proper control of the reduction in the valence states is critical in surface engineering for controlling catalytic reactions.

ACS OMEGA, 2022. DOI: 10.1021/acsomega.2c04259, Acesso Antecipado: Sept. 2022

[P249-2022] "Variable Interfacial Water Nanosized Arrangements Measured by Atomic Force Microscopy"

Teschke, O.\*; Castro, J. R.\*; Gomes, W. E.; Soares, D. M.\*

While there seems to be broad agreement that cluster formation does exist near solid surfaces, its presence at the liquid/vapor interface is controversial. We report experimental studies we have carried out on interfacial water attached on hydrophobic and hydrophilic surfaces. Nanosized steps in the measured force vs distance to the surface curves characterize water cluster profiles. An expansion of the interfacial structure with time is observed; the initial profile extent is typically similar to 1 nm, and for longer times expanded structures of similar to 70 nm are observed. Our previous results showed that the interfacial water structure has a relative permittivity of epsilon asymptotic to 3 at the air/water interface homogeneously increasing to epsilon 80 at 300 nm inside the bulk, but here we have shown that the interfacial dielectric permittivity may have an oscillating profile describing the spatial steps in the force vs distance curves. This low dielectric permittivity arrangements of clusters extend the region with epsilon asymptotic to 3 inside bulk water and exhibit a behavior similar to that of water networks that expand in time.

ACS OMEG, 2022. DOI: 10.1021/acsomega.2c01982, Acesso Antecipado: Aug. 2022

[P250-2022] "Whole-body tumor burden in PET/CT expert review"

Santos, D. F.; **Takahashi, M. E.\***; Camacho, M.; Lima, M. D. L. de; Amorim, B. J.; Rohren, E. M.; Etchebehere, E.

Introduction PET/CT whole-body tumor burden (WBTB), as a measure for overall burden of cancer, has been shown bear a strong correlation with prognosis. In the last decade, there has been significant progress in WBTB determination because of software advances and the increasing availability of positron--emitting radiopharmaceuticals. However, the determination of tumor burden with PET/CT is still a challenge especially in widespread metastatic disease. Methods In this non-systematic review, we will discuss the current role of determination of WBTB in cancer such as non-small cell lung cancer, lymphoma, breast cancer, among others and with a variety of radiotracers. Furthermore, we will address imaging techniques and quantification methods available and challenges. Results Many types of segmentation methods and different thresholds according to tumor types and radiotracers can be applied. These variations may show different WBTB results, but in general, despite variations, WBTB determination for staging purposes in lung cancer, breast cancer, lymphoma, melanoma, prostate cancer and neuroendocrine tumors have shown to bear a strong correlation with patient prognosis. Conclusion PET/CT whole-body tumor burden has an invaluable potential to assess prognosis. The accelerated radiopharmaceutical development will provide molecules and mechanisms to determine WBTB with advanced imaging qualification tools to further adjust radiotherapeutic doses in oncology. WBTB will most likely only become routinely accessible in clinical practice when fully automated programs become available and standardized.

CLINICAL AND TRANSLATIONAL IMAGING, 2022. DOI: 10.1007/s40336-022-00517-5, Acesso Antecipado: Aug. 2022

#### Artigos de eventos

[P251-2022] "Can Dynamic Functional Connectivity Be Used to Distinguish Between Resting-State and Motor Imagery in EEG-BCIs?"

Rodrigues, P. G.; **Stefano Filho, C. A.\***; Takahata, A. K.; Suyama, R.; Attux, R.; Castellano, G.\*; Sato, J. R.; Nasuto, S. J.; Soriano, D. C.

Benito RM; Cherifi C; Cherifi H; Moro E; Rocha LM; Sales-Pardo M. (Ed.)

Graph theory has been widely and efficiently applied to characterize brain functioning, ranging from the diagnosis of pathologies (e.g. depression, Alzheimer, schizophrenia, etc.) to investigations of cognitive processes in neuroscience. Recently, the use of graph-based strategies through functional connectivity (FC) analysis has shown to be an interesting option for feature extraction in motor imagery brain-computer interfaces (MI-BCIs) - an alternative communication system that does not require the use of classical biological efferent pathways, mapping brain signals directly to control external assistive devices. Although FC has been used in such context, the dynamics of FC under motor imagery has rarely been taken into account, which outlines an essential requirement for online BCI operation. Therefore, this study aims to evaluate the applicability of dynamic functional connectivity (dFC) to differentiate resting-state and motor imagery in electroencephalography (EEG)-based BCI. We evaluated the classification performance of classical markers, as defined by event-related desynchronization, static FC and the dynamic FC scenario. The analysis includes two different similarity criteria for estimating the FC matrix and four different graph-based metrics applied to a representative EEG dataset with 35 subjects. The obtained results point to the potential and accompanying challenges of using dFC in the context of MI-BCIs, in addition to providing insights concerning the motor network activity organization during motor imagery.

COMPLEX NETWORKS & THEIR APPLICATIONS X, VOL 2 Série de livros: Studies in Computational Intelligence, Volume: 1016, Páginas: 688-699, 2022. DOI: 10.1007/978-3-030-93413-2\_57

[P252-2022] "Detailed Monte Carlo simulation of energy integrating and photon counting semiconductor detectors"

Mendesa, H. R.\*; Tomal, A.\* Zhao W.; Yu L. (Ed.)

X-ray imaging techniques widely employ semiconductor detectors. Energy integrating (EI) detectors are used in digital radiography and photon counting (PC) in CT. This work aims to implement a detailed Monte Carlo modeling of these sensors. The model was divided into radiation interaction and electron-hole pairs (EHP) creation and dispersion. The PENELOPE code simulated the radiation transport. In each electron interaction, the absorbed energy was converted into EHP considering the pair creation energy and the Fano factor. The detection position was sampled using a Gaussian distribution, where the standard deviation was from the Einstein diffusion equation. The Hetch equation models the charge trapping. In the PC mode, the photon was counted if the energy deposited was higher than a threshold (ethr). Monoenergetic pencil beams between 10 and 100 keV were simulated, with 107 histories. The detector material was cadmium tellurite, with 50 mu m pixel size, whose thicknesses, applied electric field, and ethr vary, respectively from 250 to 1000 mu m, 0.01 to 1 V/mu m, and from 1 to 50 keV. The results show a wider detector response as the beam energy increases. For energies above 32 keV the fluorescence is greatly responsible for this spread. The detector's efficiency increases with the sensor thickness and decreases with the photon energy. Charge trapping decreases the efficiency up to 43,53%. For the PC mode, an ethr increase yields a narrower detector response and increases the image noise. This study provides a detailed detector modeling and, consequently, insight into the imaging system's fundamental limitations.

MEDICAL IMAGING 2022: PHYSICS OF MEDICAL IMAGING Série de livros: Proceedings of SPIE, Volume: 12031, Número do artigo: 120314Q, 2022. DOI: 10.1117/12.2607891

[P253-2022] "Electronic Nose based on Poly(vinylidene fluoride)-modified Nanofibers for Discriminative Detection of Volatile Organic Compounds"

Braunger, M. L.; Gois, B. H. de S.; Fier, I.; Oliveira, V. J. R. de; Agostini, D. L. da S.; Riul, A.\*; Olivati, C. de A. IEEE

Two e-nose setups formed by similar sensing units based on nanofibers and drop-cast films of poly(vinylidene fluoride) (PVDF) were compared. In both setups, the sensing units were formed by pristine PVDF and PVDF modified with conducting polymers. The e-noses were tested in a custom-made chamber with volatile organic compounds (VOCs) and ammonia, using dry nitrogen as a flow gas. Overall, both e-nose devices discriminate against almost all vapors, especially ammonia. The results suggest that the e-nose based on nanofibers can distinguish ethanol from isopropanol, which is not possible with the e-nose based on drop-cast films of the same materials.

2022 IEEE INTERNATIONAL SYMPOSIUM ON OLFACTION AND ELECTRONIC NOSE (ISOEN 2022), 2022. DOI: 10.1109/ISOEN54820.2022.9789622

## Artigos aceitos para publicação

[A002-2022] "Scalable Synthesis and Characterization of Multilayer  $\gamma\text{-Graphyne},$  New Carbon Crystals with a Small Direct Band Gap"

Desyatkin, V. G.; Martin, W. B.; Aliev, A. E.; Chapman, N. E.; Fonseca, A. F.\*; Galvão, D. S.\*; Miller, E. R.; Stone, K. H.; Wang, Z.; Zakhidov, D.; Limpoco, F. T.; Almahdali, S. R.; Parker, S. M.; Baughman, R. H.; Rodionov, V. O.

γ-Graphyne is the most symmetric sp2/sp1 allotrope of carbon, which can be viewed as graphene uniformly expanded through the insertion of two-carbon acetylenic units between all the aromatic rings. To date, synthesis of bulk γ-graphyne has remained a challenge. We here report the synthesis of multilayer y-graphyne through crystallization-assisted irreversible cross--coupling polymerization. A comprehensive characterization of this new carbon phase is described, including synchrotron powder X-ray diffraction, electron diffraction, lateral force microscopy, Raman spectroscopy, infrared spectroscopy, and cyclic voltammetry. Experiments indicate that γ-graphyne is a 0.48 eV band gap semiconductor, with a hexagonal a-axis spacing of 6.88 Å and an interlayer spacing of 3.48 Å, which is consistent with theoretical predictions. The observed crystal structure has an aperiodic sheet stacking. The material is thermally stable up to 240 °C but undergoes transformation at higher temperatures. While conventional 2D polymerization and reticular chemistry rely on error correction through reversibility, we demonstrate that a periodic covalent lattice can be synthesized under purely kinetic control. The reported methodology is scalable and inspires extension to other allotropes of the graphyne family.

Journal of American Chemical Society 144[39], 17999-18008, 2022. DOI: 10.1021/jacs.2c06583

[A003-2022] "High performance of carbon nanotube elastocaloric refrigerators over a large temperature span"

Silva, T. N. Y.\*; Fonseca, A. F.\*

Compression of greenhouse gases still dominates the market of refrigeration devices. Although well established and efficient, this technology is neither safe for the environment nor able to be scaled down to nanoscale. Solid-state cooling technologies are being developed to overcome these limitations, including studies at nanoscale. Among them, the so-called elastocaloric effect (eC) consists of the thermal response  $\Delta T$  of a material under strain deformation. In this work, fully atomistic molecular dynamics simulations of the eC in carbon nanotubes (CNTs) are presented over a large temperature span. The efficiency of the CNTs as solid refrigerators is investigated by simulating their eC in a model of refrigerator machine running under Otto-like thermodynamic cycles (two adiabatic expansion/contraction plus two isostrain heat exchange processes) operating at temperatures TO ranging 300-2000 K. The coefficient of performance (COP), defined as the ratio of heat removed from the cold region to the total work performed by the system per thermodynamic cycle, is calculated for each value of TO. Our results show a nonlinear dependence of  $\Delta T$  on TO, reaching a minimum value of about 30 K for TO between 500 and 600 K, then growing and converging to a linear dependence on TO for large temperatures. The COP of CNTs is shown to remain about the same and approximately equal to 8. These results are shown to be weakly depend on CNT diameter and chirality but not on length. The isothermal entropy change of the CNTs due to the eC is also estimated and shown to depend nonlinearly on TO values. These results predict that CNTs can be considered versatile nanoscale solid refrigerators able to efficiently work over a large temperature span.

PHYSICAL REVIEW B 106, 165413, 2022. DOI: 10.1103/Phys-RevB.106.165413

\*Autores da comunidade IFGW Fonte: Web of Science on-line (WOS)

#### Defesas de Dissertações do IFGW

[D020-2022] "Estudo da medição de bárions multi charmosos em colisões Pb-Pb com ALICE 3 no LHC"

Aluno: Rafaela Ramos Sarmento

Orientador: Prof. Dr. David Dobrigkeit Chinellato

Data: 07/10/2022

[D021-2022] "Estudando o impacto do tamanho do núcleon em colisões de íons pesados relativísticos"

Aluno: João Paulo Picchetti Orientador: Prof. Dr. Jun Takahashi

Data: 14/10/2022

[D022-2022] "Skyrmions Magnéticos em Multicamadas Antiferromagnéticas Sintéticas"

Aluno: Lucas Scaranari Palhares Orientador: Profa. Dra. Fanny Béron

Data: 31/10/2022

[D023-2022] "Diagnósticos de feixe de Raios-X usando pticografia para alinhamento de elementos ópticos"

Aluno: Sérgio Augusto Lordano Luiz Orientador: Profa. Dra. Alessandra Tomal

Data: 03/11/2022

[D024-2022] "Modelos Cosmológicos e Introdução às Oscilações Acústicas Bariônicas"

Aluno: Idaiane Leandra Machado Orientador: Profa. Dra. Flávia Sobreira

Data: 11/11/2022

[D025-2022] "Aplicações do Método de Beam Based Alignment para o Anel de Armazenamento do Sirius"

Aluno: Alexandre Béo da Cruz

Orientador: Prof. Dr. Antonio Rubens Britto de Castro

Data: 16/11/2022

#### Defesas de Teses do IFGW

[T016-2022] "Supercondutividade local e magnetismo em Cloreto de Cobre oxidado"

Aluno: Dyvison Pedreira Pimentel

Orientador: Prof. Dr. Iakov Veniaminovitch Kopelevitch

Data: 23/09/2022

[T017-2022] "Investigação de mudanças cerebrais decorrentes de treinamentos com realidade virtual"

Aluno: Jamille Almeida Feitosa

Orientador: Profa. Dra. Gabriela Castellano

Data: 28/09/2022

[T018-2022] "Estados eletrônicos ordenados em óxidos com estrutura ludwigitae trirutilo"

Aluno: Carlos William Galdino

Orientador: Prof. Dr. Eduardo Granado Monteiro da Silva

Data: 29/09/2022

[T019-2022] "Medição quantitativa da composição química de pequenas nanopartículas por STEM-EDS e Machine Learning"

Aluno: Murilo Henrique Martinez Moreira Orientador: Prof. Dr. Varlei Rodrigues

Data: 30/09/2022

[T020-2022] "Neutrinos na Terra e através da galáxia: fundamentos quânticos, fenomenologia e astrofísica"

Aluno: Yago Philippe Pôrto Silva

Orientador: Prof. Dr. Orlando Luis Goulart Peres

Data: 18/10/2022

[T021-2022] "Crescimento de nanoestruturas de carbono e grafeno dopado via métodos bottom-up"

Aluno: Nataly Zaribeth Herrera Reinoza Orientador: Prof. Dr. Abner de Siervo

Data: 20/10/2022

[T022-2022] "Busca por interações de contato em neutri-

nos: produção e detecção" Aluno: Mariano Esteves Chaves

Orientador: Prof. Dr. Orlando Luis Goulart Peres

Data: 31/10/2022

Fonte: Portal IFGW/Pós-graduação - Agenda de Colóquios,

Defesas e Seminários.

**Disponível em:** http://portal.ifi.unicamp.br/pos-graduacao

# **Abstracta**

Instituto de Física

Diretora: Profa. Dra. Mônica Alonso Cotta

Diretor Associado: Prof. Dr. Marcos Cesar de Olivei-

ra

Universidade Estadual de Campinas - UNICAMP

Cidade Universitária Zeferino Vaz 13083-859 - Campinas - SP - Brasil

e-mail: secdir@ifi.unicamp.br Fone: +55 19 3521-5300

### **Publicação**

Biblioteca do Instituto de Física Gleb Wataghin http://portal.ifi.unicamp.br/biblioteca

Instagram: @bif.unicamp Telegram: t.m/bifunicamp

Diretora Técnica: Sandra Maria Carlos Cartaxo

Coordenadora da Comissão de Biblioteca: Profa. Dra. Arlene

Cristina Aguilar

Elaboração:

Maria Graciele Trevisan (Bibliotecária) contato: infobif@ifi.unicamp.br